Advanced statistical analysis of vortex-induced vibrations in suspension bridge hangers with and without Stockbridge dampers

G. Bacci[a,*], Ø.W. Petersen[a], V. Denoël[b], O. Øiseth[a]

[a]NTNU, Norwegian University of Science and Technology, 7491 Trondheim, Norway
[b]ULiège, University of Liège, 4000 Liège, Belgium

Abstract

This paper presents a detailed statistical analysis of strong hanger vortex-induced vibrations (VIV) at the Hålogaland Bridge in Narvik, Norway. Severe VIV during construction led to the installation of Stockbridge dampers post-completion. Unfortunately, many dampers broke within a year, prompting a long-term measurement campaign. The measurements highlight the complexity of observed VIV, with non-stationary and multi-frequency vibrations during constant wind speeds. The paper assesses the effectiveness of various damper configurations on the hangers and finds that a single damper notably reduces vibration amplitudes, however, installing more dampers results in a lower observed difference. The research includes a detailed statistical analysis of wind data and cable responses, considering different observation intervals since the observed time of development of lock-in vibrations might impact the VIV statistical indicators. It is also shown that the duration over which wind can be considered stationary most often differs from the conventional 10-minute duration. Finally, using statistical hypothesis testing, it is demonstrated that VIV metrics are independent of the observation interval length, and it is confirmed that high turbulence intensity significantly limits the amplitude reached at synchronization. Overall, this research provides valuable insights into understanding and addressing challenges related to measuring and interpreting vortex-induced vibrations on hangers.

Keywords: vortex-induced vibration; suspension bridge hangers; Stockbridge dampers; structural monitoring

Introduction

The spans of long suspension bridges are progressively extending in length worldwide. To address the resulting structural integrity and dynamic behaviour concerns, innovative solutions are needed. As the span increases, the length of the hangers also increases proportionally. Over the years, there has been a significant evolution in hanger designs in suspension bridges. In older structures like the Golden Gate Bridge in the USA or the Forth Road Bridge in the UK, the hangers were typically made of stranded wire loops [1]. These loops were embedded into grooves on the cable bands and connected to the deck's top chord using threaded bolts. In contrast, more recent hanger designs utilize locked coil cables or parallel wire strands. These are often coated with a high-density polyethylene layer for protection [2, 3]. The ends of these modern hangers are usually attached to the cable bands and deck anchor plates through fork socket/eye plate connections. These modern connections are characterized by significantly lower friction than their predecessors. Coupled with the characteristic lower damping ratios of super long hangers [4], the hangers are more vulnerable to wind-induced vibrations. Several studies have investigated the interaction

*Corresponding author
Email addresses: giacomo.bacci@ntnu.no (G. Bacci), oyvind.w.petersen@ntnu.no (Ø.W. Petersen), v.denoel@uliege.be (V. Denoël), ole.oiseth@ntnu.no (O. Øiseth)
URL: https://www.ntnu.edu/kt (G. Bacci)

between flexible cables and fluid flow, examining the resulting dynamic behaviour. Fundamental examples can be found in the reviews on flow-induced vibrations of bluff bodies [5], which can be rigid or free to oscillate [6–8]. Whenever a bluff body, typically a circular cylinder is submerged in a fluid flow, it causes flow separations from its surface, and the separated flow creates an unsteady wake downstream of the object. The creation of these vortices arises from the roll-up of the unstable shear layers produced during flow separation. For sub-critical Reynolds numbers (from 300 to $2 \cdot 10^5$), this occurrence leads to an alternating pressure loading on the surface of the cylinder that creates a transverse force at the vortex-shedding frequency f_{vs}. For a rigid circular cylinder, this frequency is related to the well-known Strouhal number:

$$\mathrm{St} = \frac{f_{vs} D}{U} \tag{1}$$

Here, U is the steady velocity of the fluid flow and D is the characteristic dimension of the body. The Strouhal number, for circular cylinders, is nearly constant and equal to 0.18 for Reynolds numbers in the sub-critical range [9]. Therefore, if left free to move, the body will vibrate in the cross-flow direction at a frequency equal to f_{vs}. This well-known phenomenon is called Vortex-Induced Vibration (VIV). Once the vortex-shedding frequency gets near to one of the natural frequencies of the body f_n, the phenomenon of *syncronization* or *lock-in* occurs wherein the structure undergoes near-resonance vibration, which can lead to large structural displacement. In lock-in conditions, the vortex shedding frequency deviates from the direct correlation with the Strouhal number and becomes predominantly influenced by the body's motion. This interaction between the structure and the airflow exhibits a highly nonlinear dynamic. Therefore, for small variations of the flow speed U, the shedding frequency remains "locked-in" to the structure vibration frequency f_n.

The phenomenon of lock-in is part of a nonlinear dynamic process characterized by a hysteresis loop. This aspect has been thoroughly documented in the scientific literature through forced and free vibration experiments [10, 11]. Sudden jumps in vibration amplitude characterise the observed hysteresis loop. The occurrence of the jumps is affected by whether the flow velocity is raised from lower speeds or reduced from higher speeds. The hysteresis loop could be attributed to a nonlinear stiffness or damping behaviour, thus modelling the phenomena as an elastic system [12]. However, based on the findings by Feng [10], the work by Parkinson [5] proposes that hysteresis conditioning arises from the fluid mechanics, therefore from the lift forces, rather than in the elastic system. Several researchers have achieved considerable success in approximating experimental results by modelling the wake fluid system using a nonlinear wake oscillator in conjunction with the equation of motion for a mass-spring-damper system [13–16]. Beyond wake-oscillator models, which effectively approximate the entire lock-in range, the scientific literature also extensively features single-degree-of-freedom deterministic models. Well-known contributions in this area have been made by Simiu and Scanlan [17], and Vickery and Basu [18], who model the aerodynamic forces as a function of position and velocity. While single-degree-of-freedom models offer more precise approximations of the peak amplitude during lock-in, they require specific calibration for each distinct lock-in region, contrasting with the broader applicability of wake-oscillator models.

The amplitude of the cylinder response when vibrating during lock-in and the width of the lock-in region depends strongly on the ratio between the damping and excitation forces, which is usually expressed as a reduced damping parameter. One possible representation of this ratio used in literature [19] is the Scruton number:.

$$\mathrm{Sc} = \frac{4\pi\xi_s m}{\rho D^2} \tag{2}$$

where ξ_s is the structural damping of the cylinder, m is the mass per unit length, ρ is the density of the fluid, and D is the diameter of the cylinder. As the Scruton number decreases, the lock-in is characterized by an increase in structural amplitude and occurs over a wider band of wind velocities [8, 19].

During lock-in, the vibration amplitude is usually in the order of fractions of D, and does not represent an immediate structural threat. However, this kind of periodic excitation often occurs at low wind speeds and frequent wind-induced excitation can be detrimental to the fatigue life of the structure. Therefore, it is often necessary to intervene with mitigation devices that change the system's properties, such as mass, damping, or stiffness, to prevent VIV from occurring.

In recent years, numerous field observations have been documented in the literature. Vortex-induced vibrations (VIV) have been observed in the hangers of the Xihoumen Bridge in China [20], the Akinada Bridge in Japan [21], and the Gjemnessund Bridge in Norway [22]. Wake-induced vibration, along with rain-wind-induced vibration, has also been observed in many cable-stayed bridges such as the Fred Hartman Bridge in the USA [23, 24], the Erasmus Bridge in the Netherlands [24], and in cable-stayed structures, like the cable-stayed pedestrian and bicycle roundabout in Eindhoven [25].

Various techniques have been explored to mitigate VIV in these cases. The approaches generally fall into two categories: posterior damping strategies and preventive design guidelines. The former includes control mechanisms involving the installation of devices that add damping to the vibrating cable, thereby reducing the vibrations without altering or reducing the mechanism of wind loading on the cables. Classic tuned mass dampers (TMDs), consisting of an inertial mass linked to the cable by a linear spring and a damper, are a common solution [26]. More recent proposals include eddy-current TMDs [27] and TMDs coupled with elastic spacers between the hangers [28]. Another frequently used solution is a special kind of nonlinear hysteretic damper known as Stockbridge dampers, which are normally used in overhead power lines [29–31]. Numerous studies in the literature focus on the experimental characterization and modelling of this device, using both analytical [32–34] and numerical models [35]. The latter category encompasses methods to prevent VIV by modifying the structure's aerodynamic properties. These active or passive methods focus on controlling the flow detachment from the structure to reduce vortex formation in the cable wake. Common solutions include adding surface features like bumps or spiral wires to the cable [36, 37]. Proposals for actively controlling wake flow have also been made, such as using suction flow control to suppress flow separation from the structure [38, 39], or a combination of blowing and suction [40, 41].

These vibration mitigation strategies have been extensively tested through experiments, numerical simulations, and field measurements. On cable-stayed bridges, Pearsoon et al. [42] tested the damping performance of polyethene ropes, while Kim et al. [43] experimented with a Stockbridge damper configuration during non-synoptic wind events. Main and Jones [44] measured the performance of linear dampers on the Fred Hartman Bridge in the USA. In the context of suspension bridges, Deng et al. [20] demonstrated that responses measured in the field could be replicated with wind tunnel experiments. Cantero et al. [45] showed the feasibility of detecting VIV by monitoring vibrations in the bridge's deck.

However, providing a link between theoretical and experimental results to field data measurements is challenging, primarily due to the complexity of predicting turbulence's impact on shear layer instability [7]. Some wake-oscillator models that include the effect of stochastic turbulence are present in the literature [16], but currently, such numerical models lack validation in real-life conditions. This complexity is further increased by uncertainties related to the limited number of sensors deployed in the field and to commonly adopted assumptions, such as wind field homogeneity, which may not hold for very long hangers. In addition, there is a lack of studies on the long-term performance of deployed Stockbridge dampers under a variety of operational

conditions, extending beyond dynamic tests in controlled experimental settings.

In addressing these challenges, this study focuses on field data collected from a long-term monitoring campaign on the Hålogaland Suspension Bridge. The first goal is to examine the performance of Stockbridge dampers, a commonly used option in mitigating VIV in cable bridges. The study compares different damper configurations installed on the three longest hangers of the bridge, providing practical insights into the effectiveness of mitigation strategies. By analyzing data from both damped and undamped hangers, a deeper understanding of the complex dynamics involved in VIV is gained.

To enhance the observations, an advanced statistical analysis is employed on the response and the wind data. This includes testing the independence of the statistical indicators of the hangers' response from the observation window. Additionally, the influence of turbulence intensity on the maximum response induced by vortex shedding is explored by drawing insights directly from the measured data.

Essentially, this work provides an analysis of real-world field data, offering a practical exploration of VIV in the long cables of suspension bridges and its mitigation. By combining empirical evidence and statistical analysis, valuable information is presented for processing field data related to vortex-induced cable vibration.

1. The Hålogaland bridge

Figure 1: The Hålogaland bridge.

The Hålogaland bridge (Fig. 1) is a suspension bridge located in Narvik in Northern Norway. It was completed in 2018, becoming the longest suspension bridge above the Arctic Circle. As shown in Fig. 2, the direction of the bridge is almost aligned with the North-South direction, deviating from the magnetic North by only 1.1°. The surrounding topography is dominated by steep mountainsides and fjords. Immediately South of the bridge is Fagernesfjellet which is 1272 m high, shielding the bridge from southern winds. The main span of the bridge is 1145 m and the longest hangers are about 120 meters. The deck is a closed steel box girder and it is 18.6 meters wide, supporting two traffic lanes and a bicycle and pedestrian lane. The bridge has

air-spun steel main cables and locked-coil steel hangers. Furthermore, the main cables lay in a slightly tilted plane because of the particular A-shaped towers. This causes the hangers to be slightly inclined in the vertical plane. The inclination goes from 2.8 deg for the first three hangers to almost zero degrees for the hangers in mid-span. The hangers are locked-coil strands of 70 mm diameter (Fig. 3) with high-density polyethene (HDPE) sheathing, bringing the outer diameter to 84 mm with a linear mass density of 30 kg/m [2]. The thick HDPE sheathing, instead of the traditional painting, was chosen in order to protect the hangers from the environment. However, this increased the diameter of the hangers D with only a negligible increase in mass per unit length m. As a consequence, this considerably reduced the ratio between the structural damping and the aerodynamic excitation, represented by the Scruton number in Eq. (2). With the sheathing, Sc is reduced by approximately 30% (from 94 to about 65, if the structural damping ratio of $\xi_s = 0.0015$ is considered, measured by logarithmic decrement in [3]). This change made the hangers particularly susceptible to vortex-induced vibration.

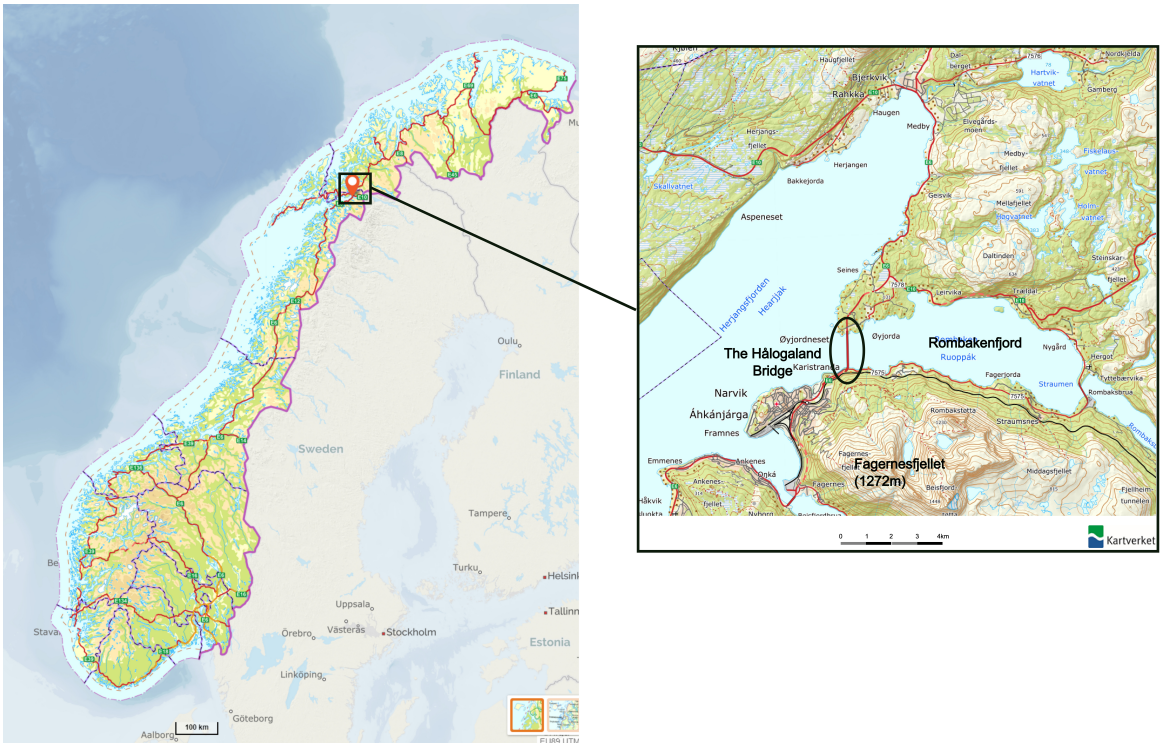

Figure 2: Location and surrounding topography (map images from Kartverket©).

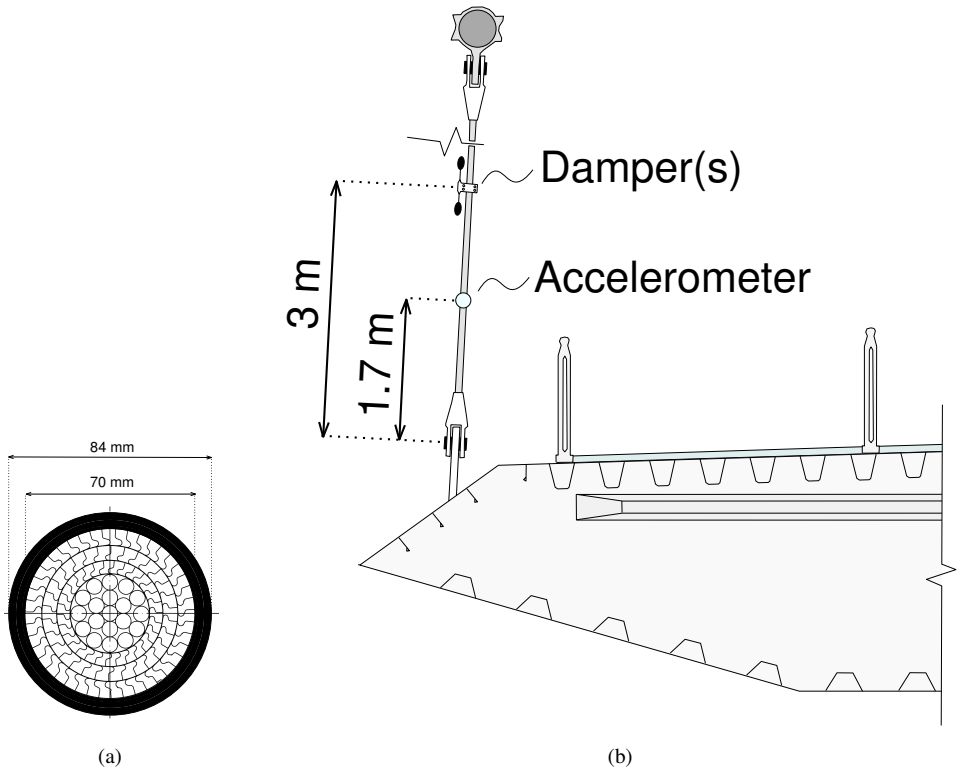

Figure 3: a) Dimensions of the locked-coil hanger with sheeting and b) placement of accelerometers and damper.

2. Monitoring of a long-span suspension bridge

2.1. A long-term monitoring project

During the construction of the Hålogaland Bridge, the longest hangers experienced strong vibrations, which continued after the project's completion. Concerns regarding the hangers' long-term durability led to the implementation of dampers on all hangers as a preventive measure. It was decided to use Stockbridge dampers (Fig. 4); this solution proved to work, significantly reducing the amplitude of vibration. However, shortly after installation, half of the installed dampers were damaged. The causes of the failure of the devices are still unclear since no structure monitoring was available at the time. However, it has been observed that the component that failed was the messenger cable near the clamp between the damper and the hanger. A similar failure mechanism has already been observed on the HPDE-coated hangers of the Çanakkale bridge in Türkiye [46].

Following this event, the whole set of about a hundred dampers has been replaced with a modified improved version provided by the supplier (Fig. 5a). Furthermore, a collaboration between the Norwegian Public Roads Administration (NPRA) and the Norwegian University of Science and Technology (NTNU) allowed the start of an extensive long-term monitoring project on cable vibration and global dynamics of the structure. The measurement campaign was started in May 2021 and continued with minor interruptions until the present time. The whole bridge was provided with a comprehensive measurement system described in detail in [47]. The present work, however, focuses on data from three accelerometers placed on the first three hangers on the South side of the bridge. The wind data is taken from the anemometer nearest to the considered hangers, as shown in the scheme in Fig. 6.

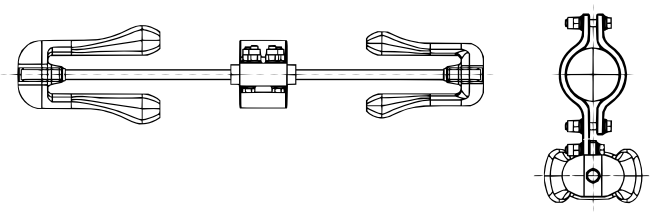

Figure 4: Drawing of the Stockbridge damper designed for the Hålogaland bridge [3].

(a) (b)

Figure 5: Sensors on the hangers: (a) triaxial piezoelectric accelerometer and two of the new dampers. (b) WindMaster 3D Pro fixed on hanger #7.

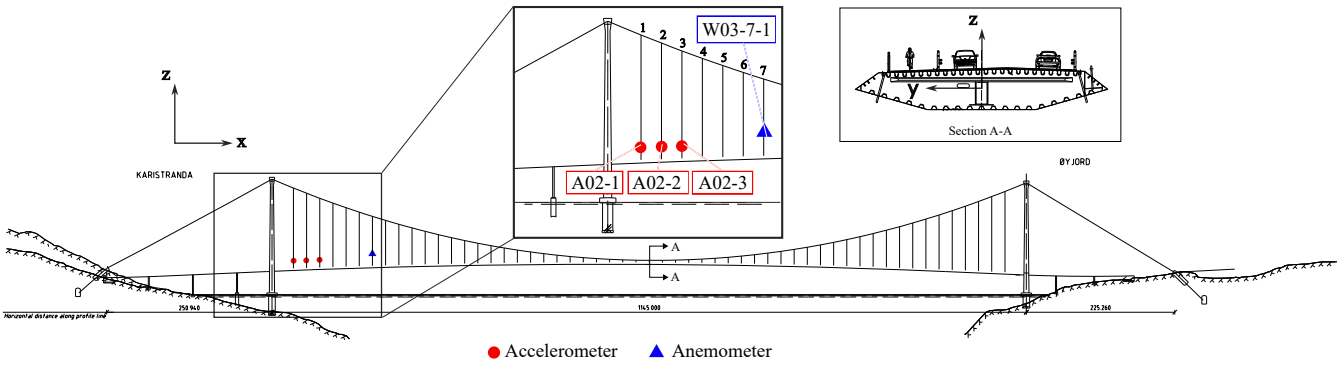

Figure 6: Scheme of the positions of the sensors on the Hålogaland bridge that are used in this work. The red circles show the accelerometers on the three longest hangers near the South tower. The blue triangles show the anemometer placed on hanger #7.

2.2. *Monitoring system and data collection*

The three triaxial accelerometers (Dytran 3063B), installed on the three longest hangers, were located 1.70 m from the lower end of each hanger. The anemometer on hanger #7, as shown in the scheme in Fig. 6, was placed at a height of 8 m above the bridge deck. Although this anemometer is located 80 m from the instrumented hangers, it is assumed that the important statistical metrics such as mean wind speeds and turbulence intensities, which will be discussed later, are representative of the locations of the hangers. This assumption is supported by the fact that in the context of wind engineering, the analysis of VIV places considerable emphasis on the system's slow dynamics [16], primarily influenced by the slowly fluctuating mean wind speed. Consequently, the slow dynamic characteristics of the wind encountered by the hangers will strongly correlate with those measured by the anemometer situated 80 meters away.

The accelerations are sampled at 200 Hz, while the anemometer data has a sampling frequency of 32 Hz. The initial Stockbridge dampers layout consisted of two dampers on each hanger, one aligned with the bridge girder and one aligned transverse to the bridge girder. However, after a storm in 2021, the first hanger was left with no dampers, the second hanger with only one in the transverse direction, and hanger #3 with both dampers undamaged. Data recording started on the 25^{th} of May 2021, shortly after most of the dampers failed. This allowed the collection of acceleration data for hanger #1 without any damper, highlighting the entity of the VIV issue and allowing for direct evaluation of the performances of two different damper configurations in the two neighbouring hangers.

In December 2021, all the dampers were replaced. The first three longest hangers, on both sides of the bridge, have been equipped with three dampers: one in the cross-bridge direction and two in the along-bridge direction. Therefore, in all the measurements following the 1^{st} of February 2022, the instrumented hangers shown in Fig. 6 are equipped with three Stockbridge dampers. As shown in Fig. 7, all three are clamped in the same location 3 m above the deck. As will be discussed in Section 3.2, this distribution might be suboptimal, since dampers' dissipative influence on the vibration modes is concentrated in one point.

The data considered in this paper extends until June 2023, with two main downtimes during the fall of 2021 and the summer of 2022, making a total of 15176 hours of available measurements.

Figure 7: New configuration of dampers for the first three hangers from February 2022.

3. Analysis of the data with standard statistical processing tools

3.1. Wind field description

Wind velocities in the present study were recorded in polar coordinates with the anemometer described in Section 2. From the measured wind data, the 10-minute mean wind magnitude $\bar{U}$ and direction $\bar{\theta}$ were determined. Next, the instantaneous wind speed has been decomposed in the alongwind and crosswind components:

$$U_u(t) = U(t)\cos(\Delta\theta(t)) \tag{3a}$$

$$U_v(t) = U(t)\sin(\Delta\theta(t)) \tag{3b}$$

Here, $U(t)$ is the instantaneous wind magnitude and $\Delta\theta(t)$ is the difference between the instantaneous direction $\theta(t)$ and the average direction $\bar{\theta}$ for the 10-minute time interval. The 10-minute averaged wind velocities for all recordings from the anemometer on hanger #7 are shown in the wind rose in Fig. 8a. From this density plot and the histogram in Fig. 8b, it can be seen how the majority of the wind data has a mean wind speed of about $6 - 7$ m/s and has either East or West as the main direction. As expected, the topography on the site makes it unlikely that winds are approaching from the North or South, where larger landmasses and mountains are located. The Westerly winds are characterized by a wider directional angle compared to the Easterly winds. The reason for this can be found in the topography surrounding the bridge site, as shown in Fig. 2. The Easterly wind is bounded by the narrow Rombaken fjord with steep mountainsides, while to the West side is a wider fjord basin which is less influenced by high mountains. From both directions, the highest 10-minute averaged wind speeds were approximately 22 m/s. The turbulence intensities in the alongwind and crosswind directions are defined as in Eq. (4), where σ_u and σ_v are the

10-minute standard deviations of the wind components U_u and U_v in Eq. (3).

$$I_u = \frac{\sigma_u}{\bar{U}}, \quad I_v = \frac{\sigma_v}{\bar{U}} \tag{4}$$

Fig. 9 shows the distribution of turbulence intensities for the whole dataset. The two distributions are very similar, with a Pearson correlation coefficient of 0.83. Therefore, in the following figures, only the crosswind turbulence intensity will be shown. Figs. 10a and 10b show the turbulence intensity as a function of wind direction and wind magnitude, respectively. In Fig. 10b, it can be seen how, for high wind velocities, the turbulence intensities converge to 10%. Most of the data points with an average wind speed greater than 5 m/s are characterized by turbulence intensities lower than 30%.

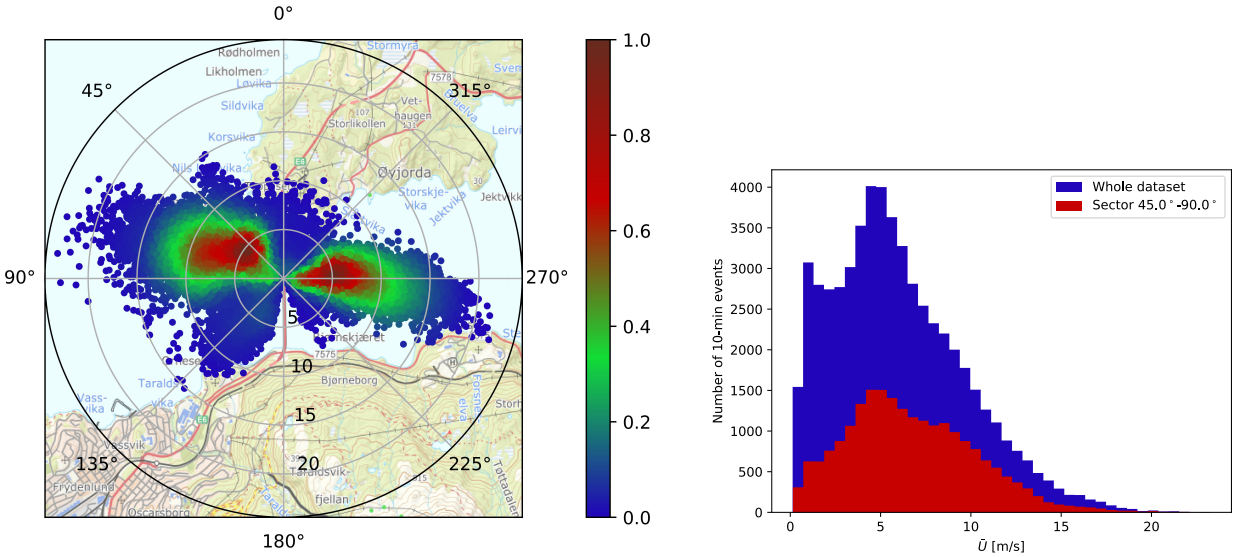

(a) (b)

Figure 8: (a) Wind-rose plot of 10-min averaged wind velocity (the colour bar indicates the relative density of the data points) and b) corresponding histogram, for the whole data set and the sector 45° − 90°, used in Section 4.2.

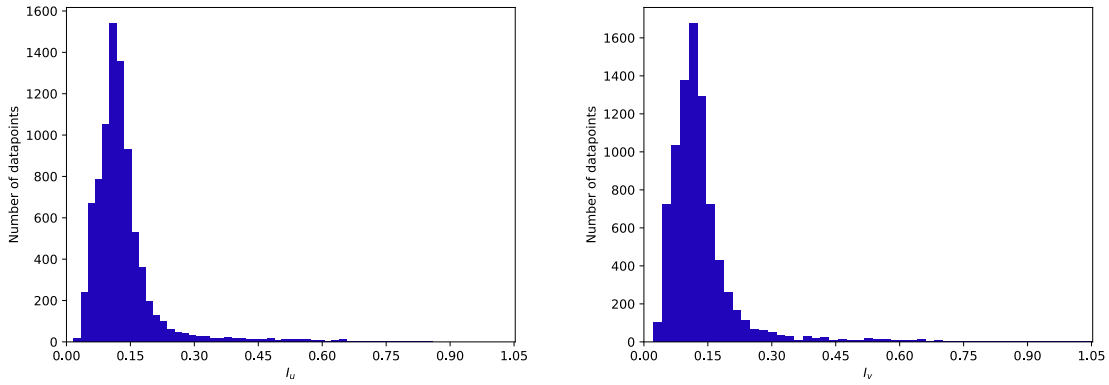

(a) (b)

Figure 9: Histogram of alongwind turbulence intensity (a) and crosswind turbulence intensity (b) of the entire data set.

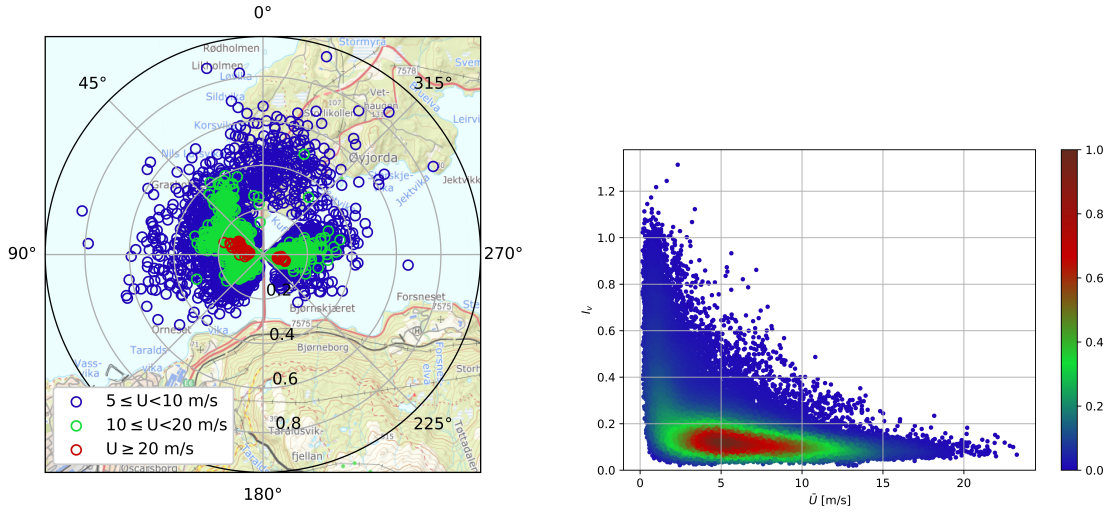

(a) (b)

Figure 10: a) Wind-rose plot of crosswind turbulence intensity I_v. b) Crosswind I_v turbulence intensity versus 10-minute mean wind speed (the colour bar indicates the relative density of the data points).

Table 1: Properties of hangers number 1, 2 and 3.

	Diameter [m]	**Tension** [kN]	**Linear mass density** [kg/m]	**Length** [m]	**Inclination** [deg]	**Fundamental frequency** f_i [Hz]
Hanger 1	0.084	1045	30	102.2	2.8	0.78
Hanger 2	0.084	966	30	111.5	2.8	0.80
Hanger 3	0.084	911	30	103.2	2.8	0.84

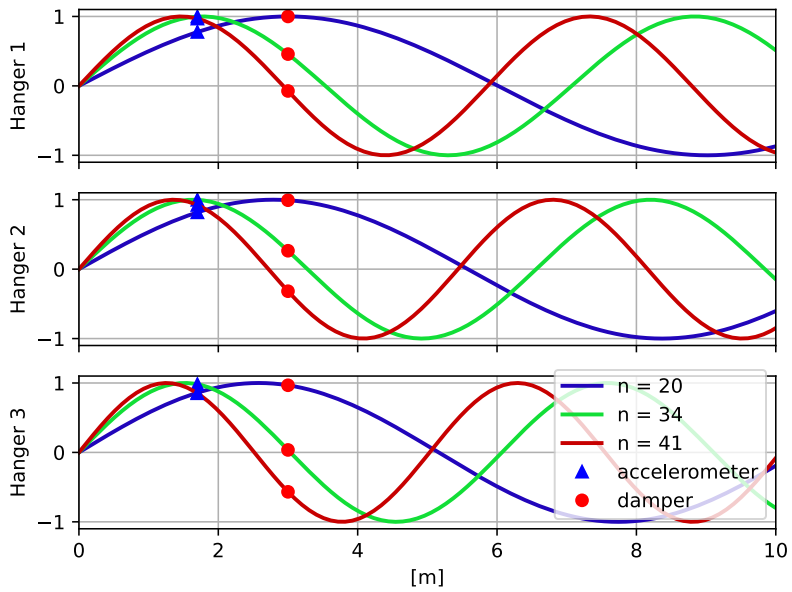

Figure 11: Examples of mode shapes of the three hangers according to taut string theory. The blue triangle and the red circle indicate, respectively, the position of the accelerometer and the dampers on each of the hangers. Here are plotted the first 10 m of the hangers. The modal frequencies are multiples of the fundamental frequency reported in Table 1.

3.2. *Dynamic response of the hangers*

In the data from the triaxial accelerometers, only the acceleration in the horizontal plane has been considered (plane $x - y$ according to the fixed reference system shown in Fig. 6). The acceleration has been transformed into a non-fixed reference system aligned with the 10-minute average wind direction denoted as alongwind and crosswind acceleration. The subsequent analysis in this work will concentrate on crosswind acceleration and displacement, as these are the primary components of vibration significantly influenced by VIV.

The spectrum analysis of the three hangers' responses facilitated the calculation of their fundamental frequencies, denoted as f_i. These frequencies were determined by the difference between two adjacent frequencies in the spectrum. The fundamental frequencies and other essential geometrical characteristics of the hangers are summarized in Table 1. According to taut string theory, the speed of bending waves propagating along the hanger is described by:

$$c = 2 f_i L \tag{5}$$

where f_i is the fundamental frequency and L is the length of the hanger. This allows to estimate the tension in the hangers due to dead load, expressed as $T = mc^2$. Assuming hinged boundary conditions, the mode shapes are given by:

$$\phi_n(x) = sin\Big(\frac{\pi}{\lambda_n} x\Big), \quad \lambda_n = L/n \tag{6}$$

Fig. 11 illustrates various vibration modes for the three hangers, highlighting the locations of the accelerometers and the dampers. The figure indicates that while the dampers effectively target certain modes, their influence is considerably less on others, given that there are potentially tenfold VIV modes. Importantly, the modal influence on the acceleration sensor varies between the modes, which in turn also affects the calculated response statistics.

In Figs. 12 and 13, two long time histories of the crosswind acceleration response of hanger #1 are shown. These time histories have been selected for the almost constant slowly varying incoming wind. Figs. 12a and 13a show also the Short-time Fourier transform of the acceleration calculated by splitting the data into segments of length 256 points (corresponding to 2 s) with an overlap of 128 points. For each segment, the spectrum is calculated with the FFT algorithm and a Hanning window is applied to reduce end effects.

Fig. 12 shows how the condition of almost constant slowly varying wind magnitude is a necessary but not sufficient condition to have a single lock-in vortex-induced vibration. Other factors govern the entrance and exit from a specific lock-in condition of the hanger, like the coherence of the wind velocity along the hanger and the change in wind direction. However, inferring further conclusions without multiple measurement points for the wind profile along the hanger is also difficult. Additionally, it can be seen that the vortex-induced response takes several minutes to reach a steady state.

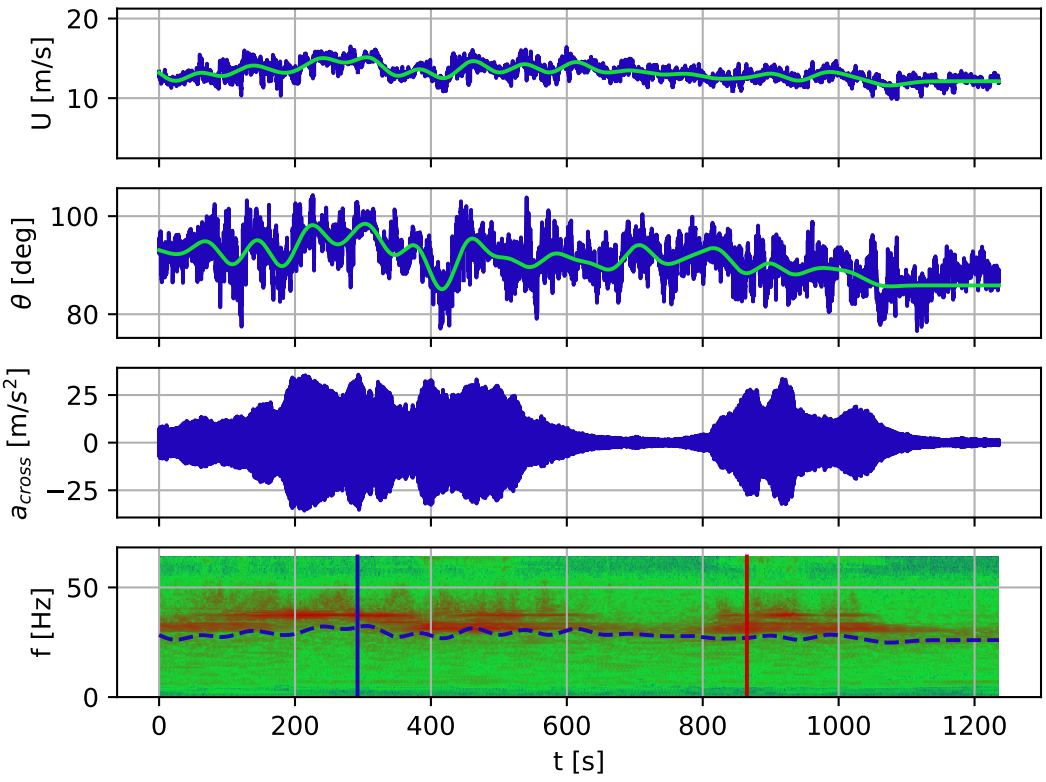

(a)

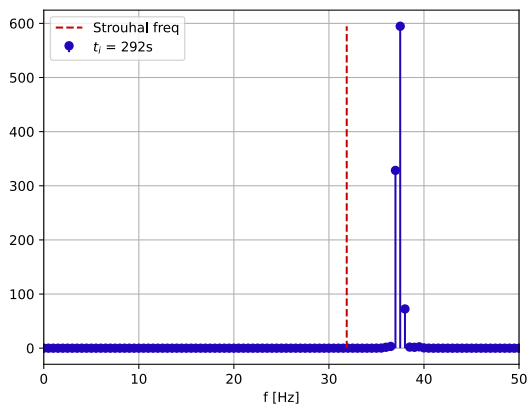

(b)

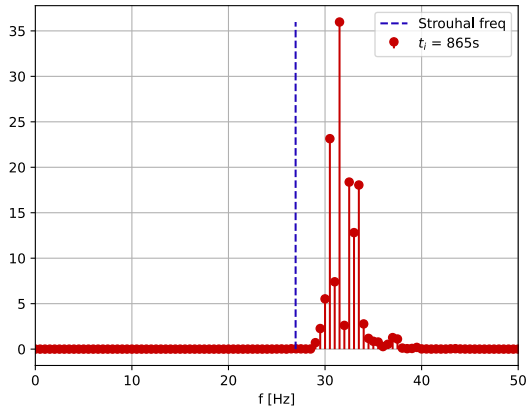

(c)

Figure 12: Sample time history recorded on hanger #1, without any damper, on 19/7/2021. a)Time history of wind magnitude U, wind direction θ from the anemometer and crosswind acceleration from the accelerometer on hanger #1 and its spectrogram. Vertical blue and red lines indicate the time instant of the spectra plotted in Figs. 12b and 12c respectively. b) Spectrum of the acceleration for the segment centred at 200 s from the beginning of the window. c) Spectrum of the acceleration for the segment centred at 921 s from the beginning of the window.

From the spectrum depicted in Fig. 12b, corresponding to the acceleration segment centred in 292 s, the vibration is mainly monoharmonic at around 37 Hz, corresponding to mode 48. The observed frequency of vibration aligns reasonably well with the Strouhal frequency of vortex shedding, f_{vs} (Eq. (1)), indicated by the dashed line in the graph. However, a gap of approximately 5.5 Hz between the two frequencies is observed. Inverting Eq. (1), this gap corresponds to a wind speed difference of about

2.57 m/s. This variation could potentially be attributed to turbulence fluctuations occurring between the hanger and the location of the anemometer. In the second time instant reported in Fig. 12c instead, a vibration with a wider frequency content can be observed. Mode 48 is still present, but with a contribution from mode 43 (33.4 Hz) and other lower modes.

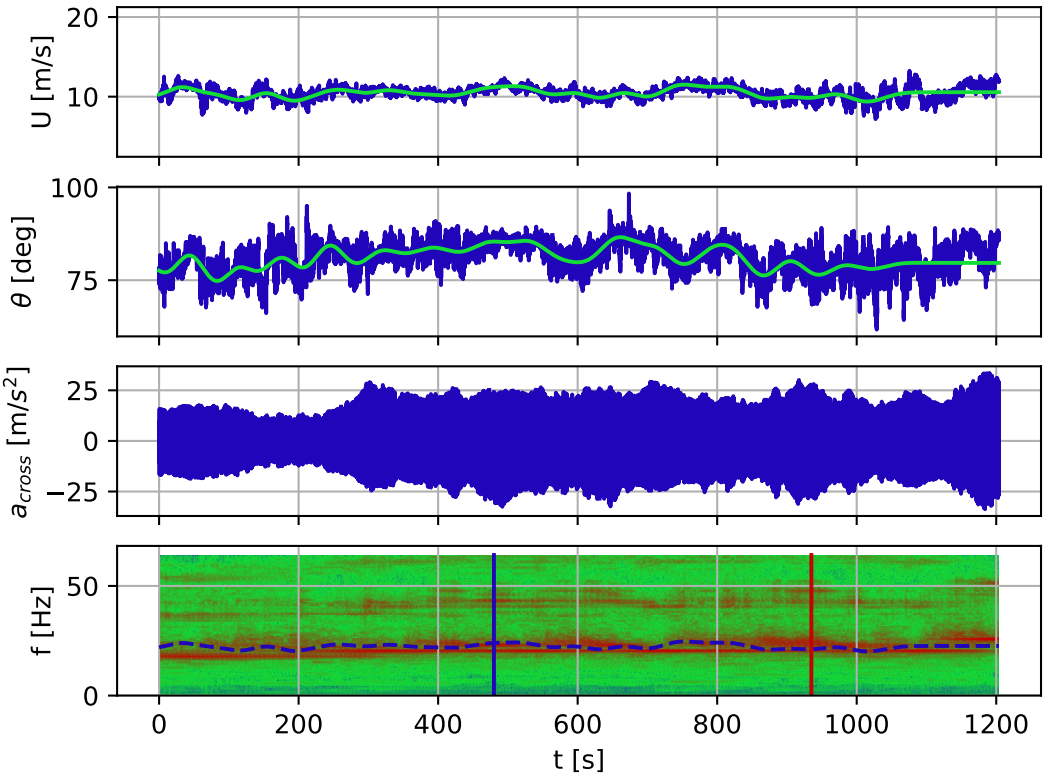

(a)

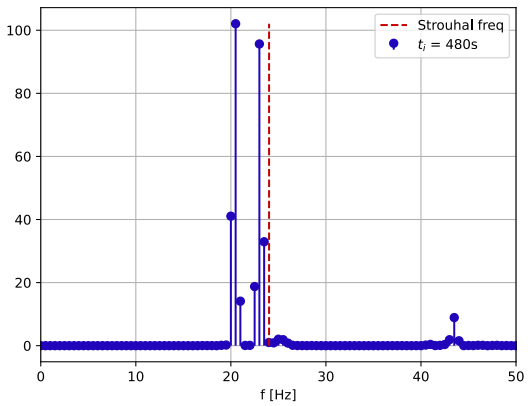

(b)

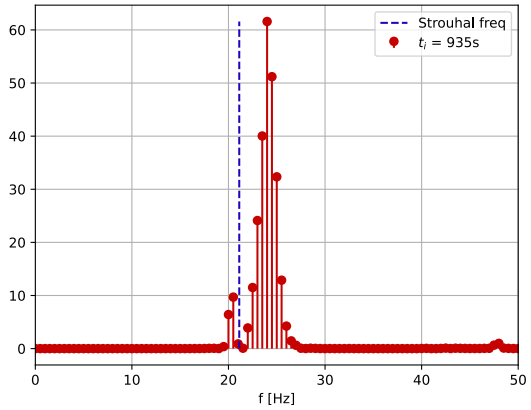

(c)

Figure 13: Sample time history recorded on hanger #1, without any damper, on 19/7/2021. a) Time history of wind magnitude U, wind direction θ from the anemometer and crosswind acceleration from the accelerometer on hanger #1 and its spectrogram. Vertical blue and red lines indicate the time instant of the spectra plotted in Figs. 13b and 13c respectively. b) Spectrum of the acceleration at 480s from the beginning of the window. c) Spectrum of the acceleration at 935s from the beginning of the window.

A second interesting example recorded the same day is shown in Fig. 13. From Fig. 13b it can be seen that the main

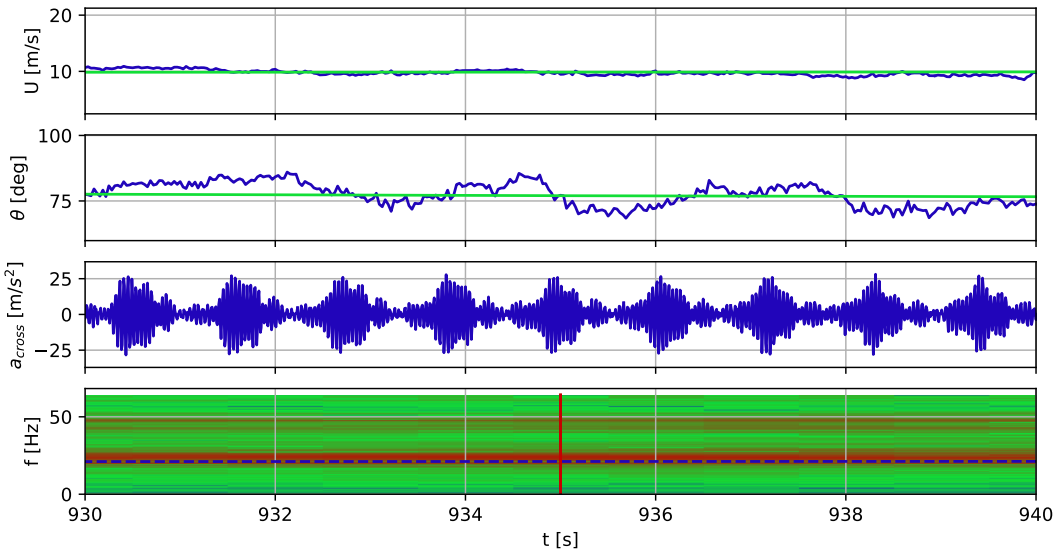

Figure 14: Portion of 10 s from the time history in Fig. 13a, corresponding to the spectrum shown in Fig. 13c.

frequency content is at about 24 Hz corresponding to mode 31, but there is also a clear component at about 20 Hz corresponding to mode 26. In this case, the vibration frequency is nearer to the theoretical Strouhal frequency for the instantaneous wind speed. In both Figs. 13b and 13c, a spectral content is also visible at about the double of the crosswind frequency of vibration: at about 44 Hz for Fig. 13b and about 48 Hz for Fig. 13c. This most likely corresponds to the inline frequency of vibration, $f_{inline} = 2f_{VIV}$.

Analysis of Figs. 13b and 13c initially suggests that the hanger is experiencing multimode vibration. Yet, the underlying physical phenomenon appears to be more complex. A closer examination, shown in Fig. 14, reveals that the hanger's behaviour is not a continuous vibration at the spectrum indicated in Fig. 13c.

Instead, the hanger displays a dynamic behaviour of alternating between frequencies, characterized by periodic frequency shifts. This pattern involves groups of vibrations, each consisting of approximately 20 cycles at a consistent frequency. After this period, the vibrations diminish and then shift to another nearby frequency. This process is then repeated. These observations underscore the complexity of the VIV response, which deviates from the traditional monoharmonic patterns. This behaviour could be linked to the influence of vortex waves propagating along the hanger, moving from regions of high wind velocity to those of lower velocity [48].

3.3. Statistics of hangers' VIV

Statistics have been derived by processing the acceleration data. In particular, the maximum a_{max} and the standard deviation σ_a of the acceleration response metrics of interest. The accelerations are also integrated in the frequency domain to obtain displacement time histories:

$$Y(\omega) = \frac{\ddot{Y}(\omega)}{-\omega^2} \tag{7}$$

Here, $Y(\omega)$, $\ddot{Y}(\omega)$ are the Fourier transform of the displacement and the acceleration, respectively. The Fourier transform of the acceleration $\ddot{Y}(\omega)$ is filtered with a rectangular filter with cutoff frequency 2 Hz. Then, the displacement $y(t)$ is found by taking

the inverse Fourier transform of $Y(\omega)$. For displacement, the same statistical indicators of maximum and standard deviation are calculated over intervals of 10 minutes.

As explained in Section 2.2, the two years of recordings allowed a critical comparison of the effect of different damper configurations on the hangers. Fig. 15 shows the standard deviation of the displacement of hanger #1 from 2021, when it had no dampers, to the following period when three dampers were installed, as a function of the 10-minute averaged wind speed. The introduction of three dampers into the system resulted in the elimination of the lock-in peak at 7 m/s and a reduction of the maximum displacement of about 80%. However, the difference between the configuration with one and three dampers is less evident. This comparison can be seen on hanger #2 in Fig. 16a. It is also interesting to notice how adding damping to the system changes its VIV characteristics, moving the peak of the response from about 7 m/s to around 13 m/s for one damper installed and 16 m/s for three dampers installed. Currently, all the dampers have been clamped 3 m from the lower hanger anchorage (see Fig. 7). The authors aim to investigate if better performance can be achieved by optimizing the locations of the dampers [34].

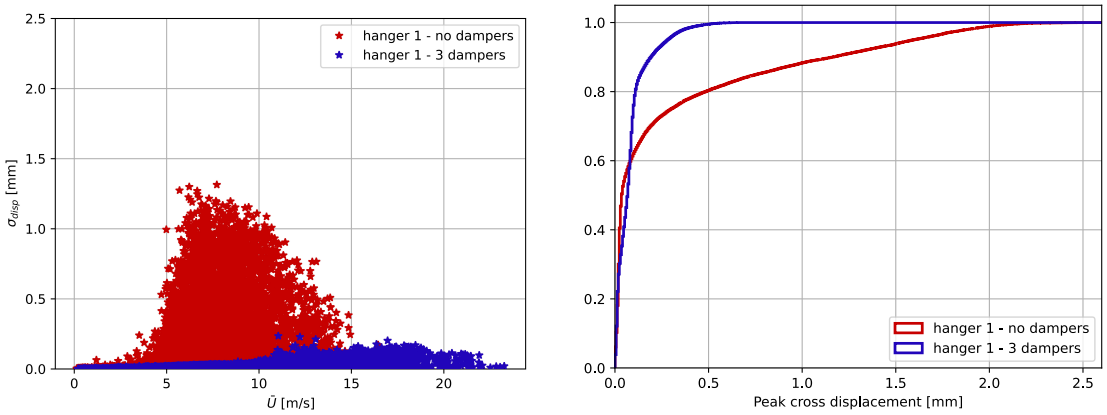

(a) (b)

Figure 15: Comparison of performances of two-damper configurations on hanger #1 through displacement at 1.7 m from hanger anchorage. (a) Scatter plot of the standard deviation of the displacement versus 10-minute mean wind velocity, (b) cumulative histogram of the peak displacement.

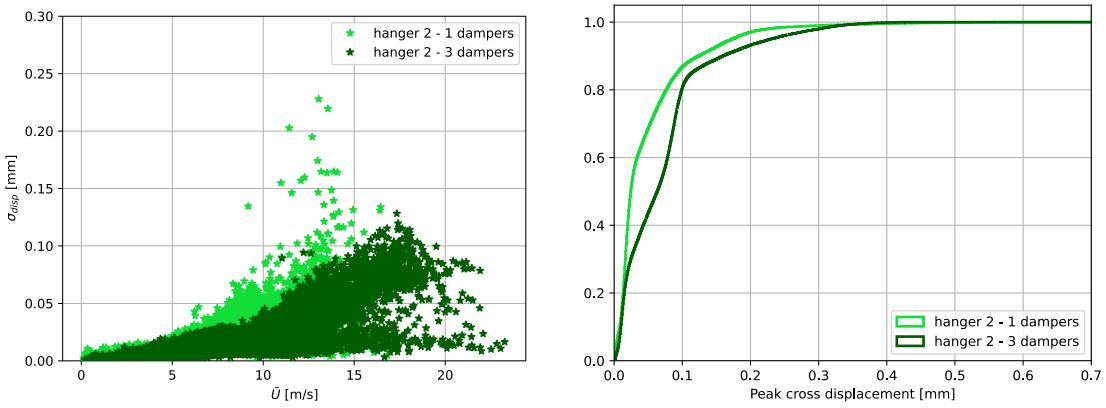

(a) (b)

Figure 16: Comparison of performances of two-damper configurations on hanger #2 using displacement at 1.7 m from hanger anchorage. (a) Scatter plot of the standard deviation of the displacement versus 10-minute mean wind velocity, (b) cumulative histogram of the peak displacement.

Finally, in Fig. 17 the statistics from all four encountered damper configurations are plotted together, both in terms of a scatter plot of the standard deviation of displacement (Fig. 17a) and in terms of a cumulative distribution of the maximum displacement (Fig. 17b). The difference in damping effectiveness from the undamped hanger to the hanger with three dampers can easily be observed. It must be highlighted that, from Fig. 17a, the solution with three dampers on hanger #1 seems less effective than the solution with two dampers on hanger #3. This is only caused by the fact that the accelerometers are all placed at the same height of 1.7 m, regardless of the hanger. For example, given a wind speed of 15 m/s, the 41^{st} mode is excited on hanger #1. For this mode the accelerometer position corresponds to 97% of the maximum amplitude point, see Fig. 11. While on the slightly shorter hanger #3, the 38^{th} mode is excited. For this hanger, the accelerometer position corresponds to only 92% of the point of maximum amplitude, resulting in a smaller perceived displacement through the measurements.

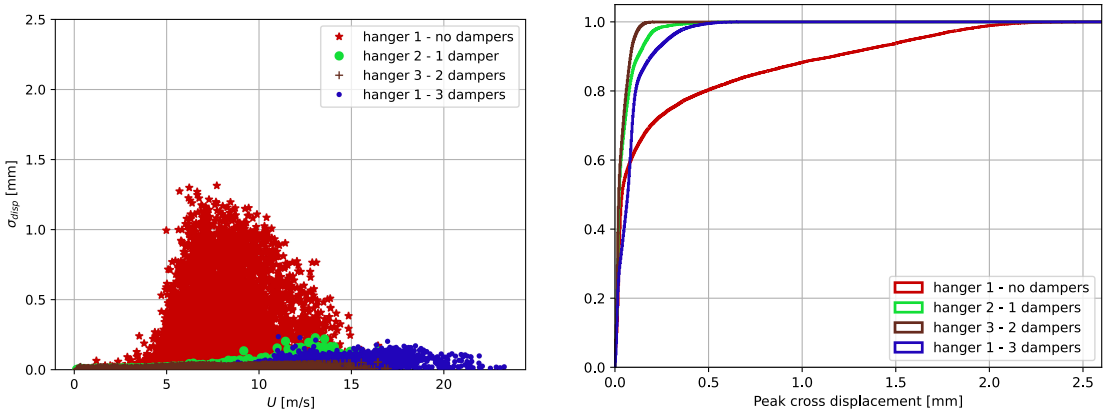

(a) (b)

Figure 17: Comparison of performances of four different damper configurations on the on the three analysed hangers through displacement at the accelerometer. (a) Scatter plot of the standard deviation of the displacement versus mean wind velocity, (b) cumulative histogram of the peak displacement.

The effect of turbulence intensity on the response can be appreciated from Fig. 18, where the influence of both wind

magnitude and turbulence intensity is emphasized. At around 7 m/s, as mentioned earlier, hanger #1 without any damper shows the maximum VIV amplitude, but this seems only observable for low turbulence intensities. This is expected since, with little turbulence, a coherent vortex detachment along the hanger can be generated more easily, and therefore, a precise frequency is excited for a longer time, enabling it to enter the lock-in limit cycle with the highest displacement. When turbulence is high, the coherent vortex-shedding is continuously disturbed, resulting in a lower maximum displacement [16].

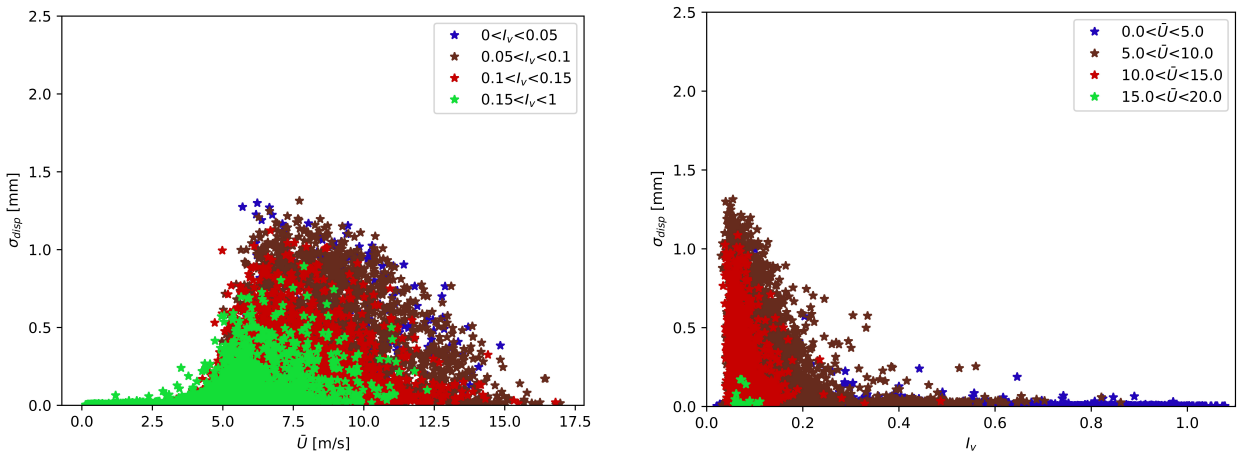

(a) (b)

Figure 18: Standard deviation of the displacement on hanger #1 during 2021 (no damper) as function of (a) crosswind turbulence intensity and (b) wind speed. The statistics are calculated for $T = 10$ min.

The statistical indicators shown in Figs. 15 to 18 were calculated over for 10-minute intervals. Fig. 19 illustrates an example of two intervals, showing the wind magnitude and direction and the acceleration response of the three hangers. The spectrogram of hanger #1 is also shown. The spectrograms in Fig. 19 show how the frequency content of the hanger vibration closely follows the frequency of vortex-shedding f_{vs} (Eq. (1)), which is indicated with a continuous blue line. The alignment of the vibration frequency with the vortex-shedding frequency indicates that the resonance excitation witnessed can indeed be attributed to vortex-induced vibration. As shown in Section 3.2, the time required to reach a steady state for the vortex-induced response is in the order of 10 minutes. Therefore, it could easily happen, as shown in Fig. 19b, that only part of the process is included in the time interval used to calculate the statistics and the VIV episode develops across multiple intervals. Vice versa, multiple VIV episodes can be captured in the same observation interval, as shown in Fig. 19a. The consequence of this is seen in Fig. 18a, where a scatter of numerous oscillation amplitudes is observed for the same averaged wind speed.

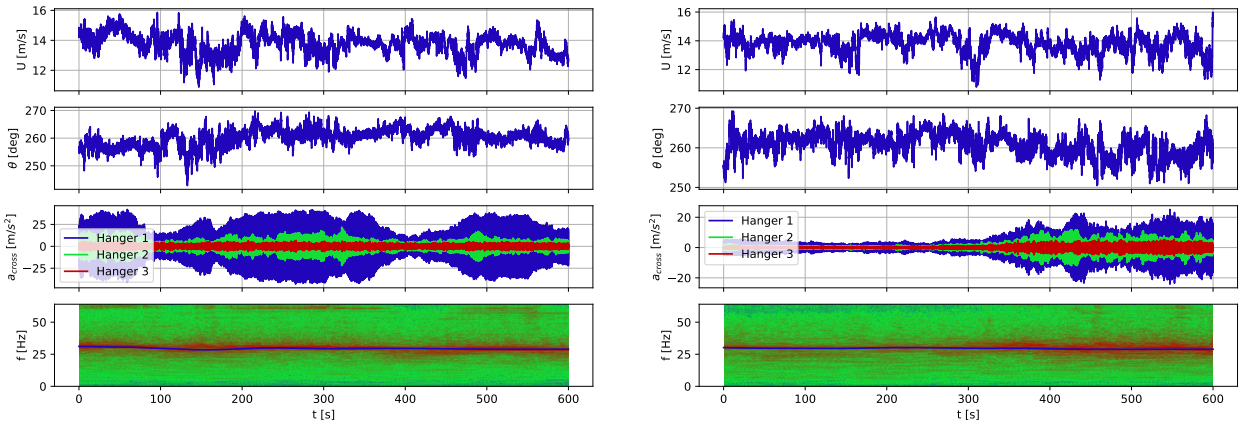

(a) Recording started 18:49.

(b) Recording started 18:38.

Figure 19: Sample time histories from 15th of June 2021. In blue, from the top, the wind magnitude, the wind direction and the crosswind acceleration of hanger 1, with no damper, hanger 2, with one damper, and hanger 3, with two dampers. In the bottom plot is shown the spectrogram of the acceleration of hanger 1. The blue line in the spectrogram shows the theoretical vortex-shedding frequency corresponding to the average wind velocity.

4. Advanced statistical methods for the analysis of time series

As highlighted in Section 3, using a fixed time interval of 10 minutes in the statistical analysis might lead to the recording of multiple growth-to-steady state VIV episodes or suffer from episodes spreading on consecutive windows. This causes, as shown in Fig. 18a, a scatter of different oscillation amplitudes for the same wind speed. If standard deterministic models, like the one proposed by Scanlan [17], were used to predict this type of response, one would expect it to cluster along the upper envelope in this diagram. The scatter is not only attributable to variability in the measurements (including the turbulence and uncertainty on the wind field) but also to the possible non-stationary nature of the acceleration records over the considered time windows of 10 minutes duration.

To investigate possible causes of this scatter, the wind data was analysed by searching for time intervals with only a small slowly varying wind variation. The method used to define almost constant slowly varying wind is described later in Section 4.1. As will be shown, for the majority of the time, the slowly varying wind is almost constant for 3 minutes or less. The fact that the slowly changing mean wind speed changes considerably within these 10-minute intervals, is critical for VIV mechanics, as they typically require a relatively steady wind velocity to develop lock-in vibrations fully. This naturally calls for a study of the influence of the time window T used to perform the statistical analysis of VIV data. This analysis is exposed in Section 4.2.

4.1. Wind data analysis

The wind data, which is continuously recorded (except for occasional system downtime), has been sliced into time intervals with almost constant slowly varying wind speeds. In this work, a time interval with almost constant slowly varying wind speed is defined as a portion of time history where the minimum u_{min} and maximum u_{max} slowly varying wind speed lies within ±15% of the average wind speed of the window, $\bar{U}$. The slowly varying wind speed is obtained by low-pass filtering the instantaneous wind speed using a 20th order Butterworth filter with a cut-off frequency of 1/60 Hz. An algorithm to identify time intervals with almost constant slowly varying wind has been developed and is presented in Algorithm 1. The algorithm initially considers

only the first sample of the wind velocity. Next, samples are added individually as long as the slowly varying wind speed at the particular time instance is within the boundaries explained above. The algorithm stops and defines the end of the time interval when the criteria are not met. An example is shown in Fig. 20, illustrating that whenever the filtered wind speed exceeds the boundaries defined by the green dashed lines, the time interval ends, and a new one is started. Time intervals with average wind less than 4 m/s have been discarded.

Algorithm 1 Inclusion of a new data point u into an almost constant slowly varying wind window

1: Initialize the window's current average $\bar{U}_{old}$, number of samples n_{old}, maximum u_{max} and minimum u_{min}.
2: Update $\bar{U}_{new} = \frac{\bar{U}_{old} n_{old} + u}{n_{old}+1}$ with the new point u
3: Update window extremes u_{max} and u_{min} with the new point u, if required.
4: **if** $(u_{max} < 1.15\bar{U}_{new})$ & $(u_{min} > 0.85\bar{U}_{new})$ **then**
5: u can be added to the window
6: $\bar{U}_{old} = \bar{U}_{new}$
7: $n_{old} = n_{old} + 1$
8: Go to 1.
9: **else**
10: Discard u and start a new window.
11: **end if**

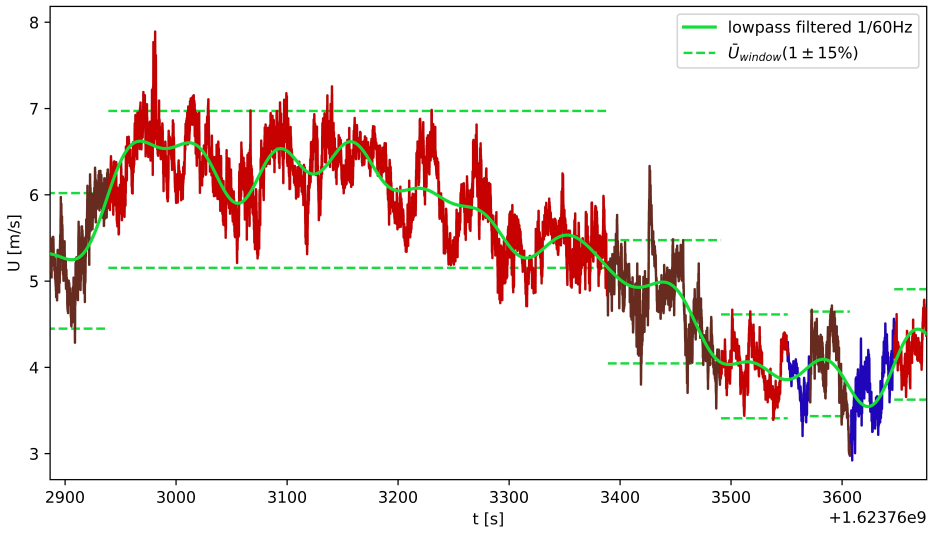

Figure 20: Example of the application of the algorithm for identification of almost constant slowly varying wind windows. The results show how both long and short windows are identified. The windows highlighted in blue are discarded as their average wind speed is below 4 m/s.

Fig. 21 shows the outcome of the described analysis in terms of the duration of time intervals with almost constant, slowly varying wind speeds. The plot shows that 50% of the time intervals are shorter than 3 minutes. Fig. 19b showed that it could also take 5 minutes for VIV to reach the limit state. This means that, in many cases, there isn't enough time for the hanger to reach a steady state before the wind speed changes. From these results, it can be seen why the long-term distribution of the response is highly skewed towards small amplitudes, with occasionally larger peaks when the lock-in limit cycle is reached, as

depicted in Fig. 18a. However, the plot in Fig. 21 also shows that there are rare instances of time intervals with almost constant, slowly varying wind that can last for 30 minutes or more.

The definition of time interval with almost constant slowly varying wind speed was formulated only concerning the magnitude of the wind vector. This choice was made for two main reasons. First, the overall wind distribution indicates a prevalence of Easterly and Westerly winds, resulting in mainly two perpendicular directions of wind incidence to the bridge. Second, given the axisymmetric geometry of the considered system, minor changes in the incidence angle were assumed to be negligible. However, it is probable that including the direction in the window definition will result in a further reduction of the average time interval length, a hypothesis which has not yet been verified.

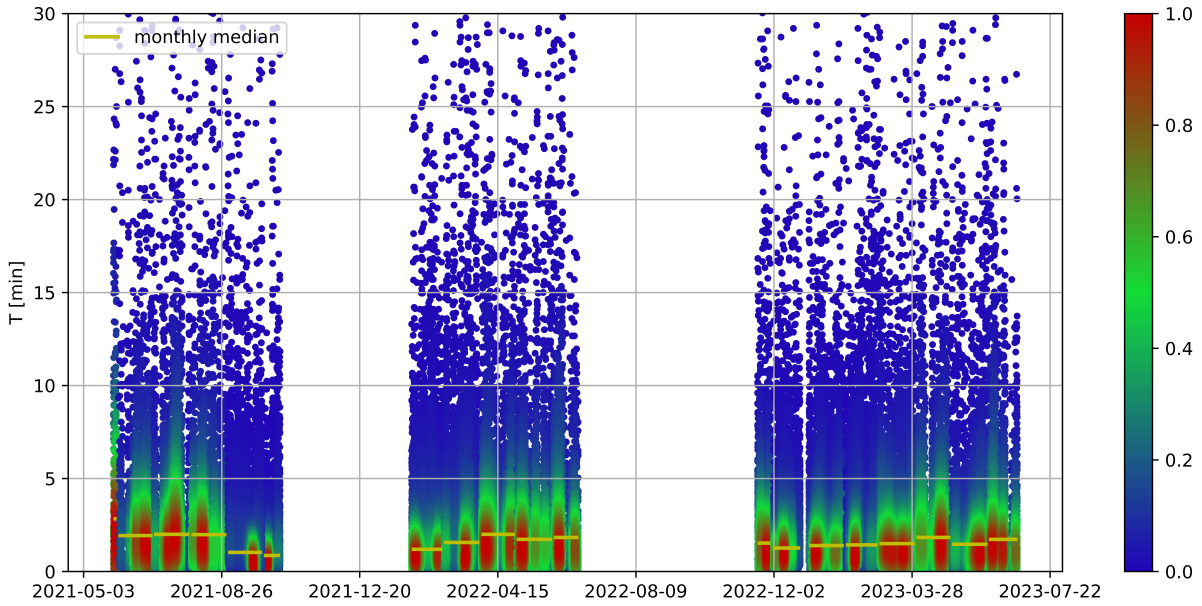

Figure 21: Length of time intervals with almost constant slowly varying wind for the whole data set. In yellow is the median value for each month. The colour bar indicates the data density.

4.2. Response analysis

The mean, maximum, and standard deviation, serving as statistical indicators of the response, are calculated across six distinct time intervals $T = \{30\text{ s}, 60\text{ s}, 5\text{ min}, 10\text{ min}\}$. This analysis seeks to determine if the statistical properties of VIV depend on the time interval T. For the sake of clarity, this section focuses on data collected from hanger #1 in the 2021 period, during which it had no damper, resulting in measured responses that are considerably large. However, this location did not correspond to the point of maximum displacement for modes 34 and lower (see Fig. 11). To ensure that mean wind direction doesn't affect the analysis, the data in this section has been limited to T-minute average wind direction from the sector 45° to 90°. This range is one of the most common directions at the site, which was shown in Fig. 8a. This range was preferred over the symmetric 45° to 135° sector because, while being narrower, it only has 15% fewer data than the symmetric sector, and the discarded points had T-minute average wind magnitude mostly below 5 m/s.

As the time interval gets shorter, the number of calculated data points increases due to the finer time resolution. However, the number of compared points should be kept the same to ensure a fair comparison across different T values. The method utilized to achieve this result can be outlined using the 10-minute dataset, referred to as the $N_{10\text{min}}$ data set, and the 30-second

dataset, the N_{30s} data set, as an example. The objective is to create a new subset from the N_{30s} set, having the same number of points as the N_{10min} set.

In this procedure, for each data point from N_{10min} set, a corresponding point from N_{30s} set, calculated from the same 10-minute period, is identified and selected. This results in a new data set, matching the number of points in the N_{10min} set but consisting of data from the N_{30s} set. In essence, this method allows for a direct and meaningful comparison between the two data sets, each originally averaged over different time scales.

These points were then plotted against the average wind speed within the interval T, hereafter referred to as $\overline{U}$. This approach yielded an experimental representation of the velocity-amplitude (V-A) curve caused by VIV [43]. Figure 22 displays two examples of such scatter plots. A preliminary qualitative assessment suggests a noticeable similarity between the two data sets at the extremities of the T interval range. This implies that calculating the statistics over different T intervals seems not to have a great influence on the final shape of the V-A curve.

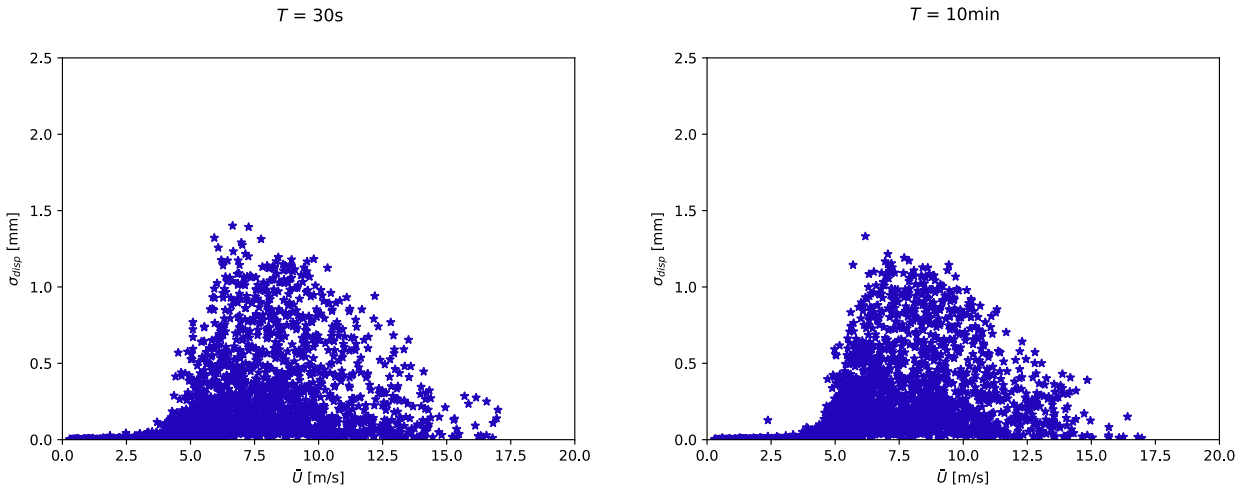

(a) (b)

Figure 22: Standard deviation of the displacement on hanger #1 during 2021 (no damper) for two different time intervals T, filtered for wind direction $45° < \bar{\theta} < 90°$.

From an engineering perspective, the primary interest in analyzing the VIV phenomenon lies in its impact on the service life of the hanger. A crucial metric in such analysis is the envelope of the standard deviation of displacement across varying wind velocities. A *backbone curve* is here defined as the 95^{th} percentile of the standard deviation of the hanger displacement, conditioned upon the window averaged wind velocity $\overline{U}_j$. In practice, this conditional requirement is implemented by calculating the average wind velocity over bins called $\overline{U}_j$ of width $\Delta U = 0.8$ m/s with the index j indicating the left edge of the bin. Such a curve exists for each observation window T_i with $i \in \{30\text{ s}, 60\text{ s}, 5\text{ min}, 10\text{ min}\}$. It is therefore denoted as $X^i_{95}(\overline{U})$, or $X^i_{95,j} = X^i_{95}(\overline{U}_j)$.

Bootstrapping techniques are employed to analyze the two sets of points by generating 1000 random samples. Each sample consists of $N_{10}/2$ points, drawn from the respective sets. For every sample thus obtained, the 95^{th} percentile backbone curve is computed. This process results in the creation of a statistical distribution for each wind speed bin $\overline{U}_j$, characterized by a mean $\overline{X}^i_{95,j}$ and a standard deviation $\sigma_{X^i_{95,j}}$. The aim of this methodological approach is to robustly estimate the statistical properties

of the 95^{th} percentile backbone curve for different wind speed conditions.

The dispersion of these 1000 envelope curves is illustrated in Figure 23 for two observation windows. In both instances, the realization of the *backbone curve* provides a reliable estimate of the build-up to resonance and predicts the onset of full lock-in wind speed.

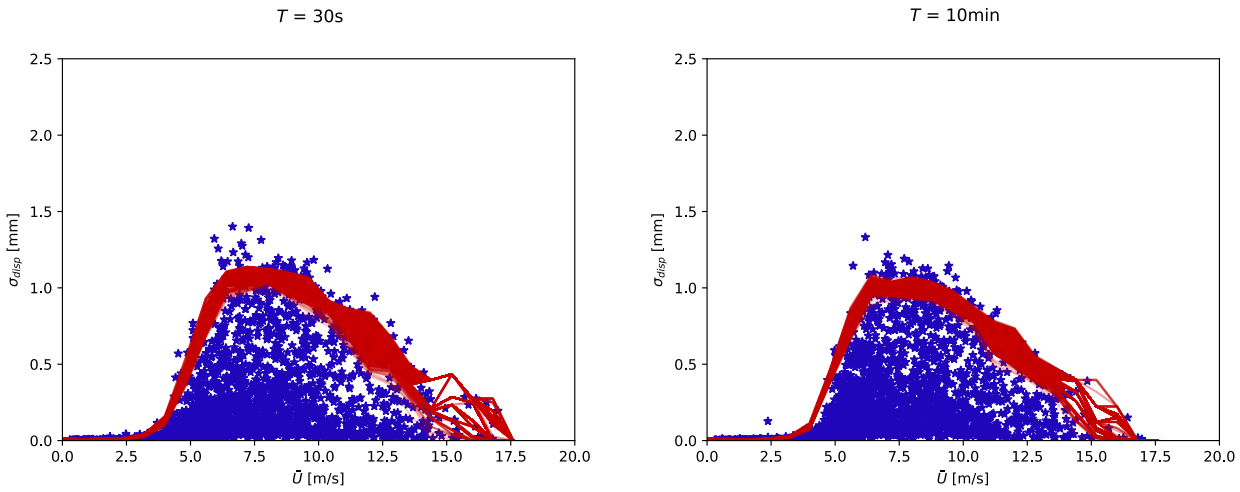

(a) (b)

Figure 23: Standard deviation of the displacement on hanger #1 during 2021 (no damper) for two different time intervals T. In red the 1000 realizations of the backbone curve X^i_{95}, with a) i = 30 s and b) i = 10 min.

To quantitatively assess the differences between the *backbone curves*, the curves X^1_{95} and X^2_{95} in Figure 23 are subjected to statistical hypothesis testing. The null hypothesis $\mathbb{H}_0$ posits that "*The means of* X^1_{95} *and* X^2_{95} *are equivalent.*" For a specific wind speed bin $\overline{U}_j$, the observed mean difference is $\hat{\Delta}_j = \left|\overline{X}^1_{95,j} - \overline{X}^2_{95,j}\right|$.

Under the assumption of $\mathbb{H}_0$, the probability of observing a difference as significant as $\hat{\Delta}_j$ is $P\left(\Delta_j > \left|\overline{X}^1_{95,j} - \overline{X}^2_{95,j}\right|\right)$. Assuming Δ_j follows a Gaussian distribution with zero mean and a standard deviation $\sigma_{\Delta,j} = \left(\sigma^2_{X^1_{95,j}} + \sigma^2_{X^2_{95,j}}\right)^{0.5}$, the p-value for each wind bin $\overline{U}_j$ is computed as $p_j = 2\left[1 - \Phi\left(\hat{\Delta}_j/\sigma_{\hat{\Delta}_j}\right)\right]$, where Φ denotes the Gaussian cumulative distribution function. The significance level is set at $\alpha = 5\%$, and the p-value is calculated for each $\overline{U}_j$, comparing the smallest and largest T in the aforementioned range.

Should $p > \alpha$ for all $\overline{U}_j$, the two *backbone curves* are statistically indistinguishable, implying that the time interval T does not affect the determination of the response's backbone.

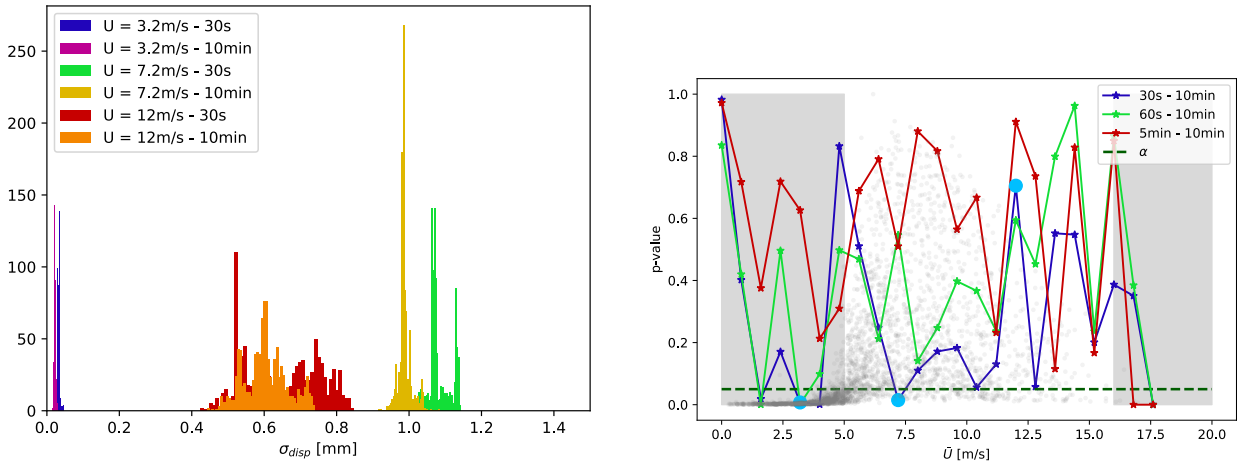

(a) (b)

Figure 24: a) Distribution of $X^i_{95_j}$ for $j = \{3.2$ m/s, 7.2 m/s, 12 m/s$\}$ and $i = \{30$ s, 10 min$\}$. b) p-values for different wind speeds for three statistical hypothesis tests. Light blue dots indicate the configurations for which the distributions are detailed in Fig. 24a. In the background, the point set is shown to guide the eye.

Figure 24a presents three instances of the 95th percentile distribution for three distinct wind speed bins $\overline{U}_j \in \{3.2, 7.2, 12\}$ m/s. Notably, the standard deviation of the percentile gets larger with increasing wind speed, attributable to the scarcity of experimental data at higher velocities. Despite this, a preliminary observation reveals a statistical similarity between the two distributions, which becomes more pronounced at higher wind speeds.

This observation is substantiated in Figure 24b, which depicts the results of a statistical hypothesis test across three time interval combinations. In particular, the 10 min data set has been compared with the 30 s, 60 s and 5 min data sets. In the wind speed range where VIV is significant and sufficient experimental data exists (specifically between 5 m/s and 16 m/s), the p-value for each wind speed bin mostly exceeds the predefined significance level of the test. The majority of test failures happen at low wind speeds for the first two comparisons Fig. 24b. It is important to note that the test is considered to fail when there is insufficient overlap between the two distributions of the 95^{th} percentile. However, the hanger's response is considerably smaller at lower wind speeds. As illustrated in Fig. 24a for the blue and violet distributions for $\overline{U}_{3.2}$, the discrepancy leading to test failures is actually on the scale of a tenth of a millimetre. For the specific application of this hypothesis test in our study, it is reasonable to disregard the failures at low wind speeds. They likely do not signify meaningful differences in the context of the broader analysis.

Consequently, the null hypothesis can be accepted, thereby confirming that the distributions X^1_{95} and X^2_{95} are statistically indistinguishable. From this analysis, it is inferred that within the wind speed range where VIV is evident for the hanger, the length of the time window does not significantly impact the representation of the response's backbone when using averaged statistics. The scatteredness of the data can be attributed to other factors.

4.3. Turbulence intensity effect on the response

In Fig. 18 it was shown the significant impact of turbulence intensity on the standard deviation statistics of the VIV response. Consequently, in conditions of high turbulence, the hanger doesn't reach the maximum displacement corresponding to the specific wind speed, primarily because high turbulence intensity tends to inhibit synchronization. To validate this hypothesis

and further evaluate the method employed in the preceding section, a second statistical hypothesis test was conducted. This test compared VIV statistics derived from data sets with varying turbulence intensities. Fig. 9 illustrates the distribution of turbulence intensities within the collected data.

The data was divided into two groups based on crosswind turbulence intensity: $I_v < 0.15$ and $I_v > 0.15$. For each group, the response envelope was calculated using the 95^{th} percentile method, as previously described, and is depicted in Fig. 25 for 1000 realizations.

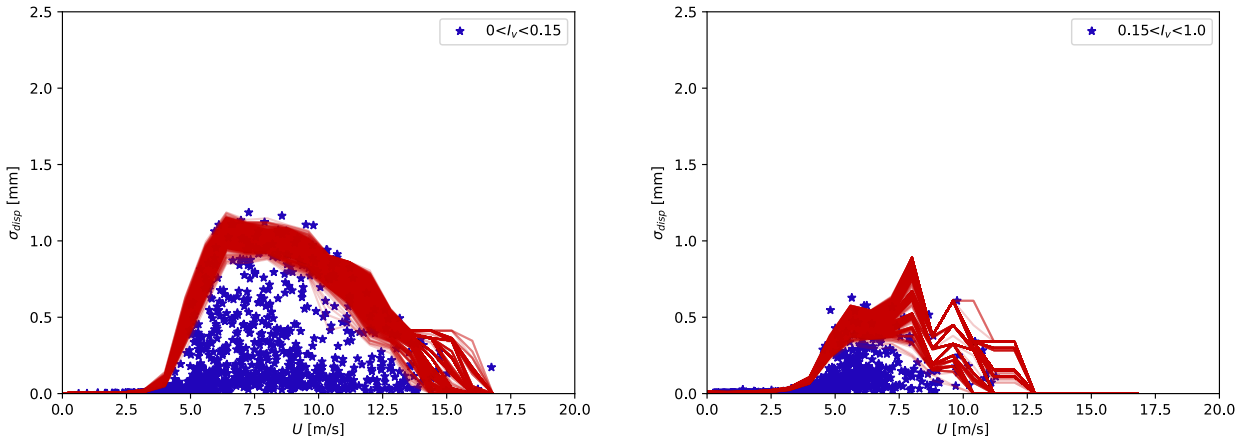

(a) (b)

Figure 25: Standard deviation of the displacement on hanger 1 during 2021 (no damper) for two different crosswind turbulence intensity intervals. In red, the 1000 realizations of the backbone curve X^i_{95}.

Fig. 26a presents three instances of the 95^{th} percentile distribution for different wind speeds $\overline{U}_j \in \{4, 7.2, 12\}$ m/s. Here, it is evident that only the distribution for $\overline{U} = 4$ m/s shows similarity in both turbulence intervals. As the wind speed increases, the higher turbulence intensity group lacks sufficient data points to accurately estimate the backbone curve. Finally, Fig. 26b displays the results of the hypothesis test, indicating that for wind speeds between 5 m/s and 16 m/s, the null hypothesis must be rejected. This finding confirms that data sets with high turbulence intensity are characterized by a lower backbone curve compared to low turbulence data for the same wind speeds.

Combining the findings of sections Sections 4.2 and 4.3, it is found that the scatteredness in the V-A curves is better explained by wind turbulence than the possible difficulties related to the co-existence of several timescales in the statistical processing.

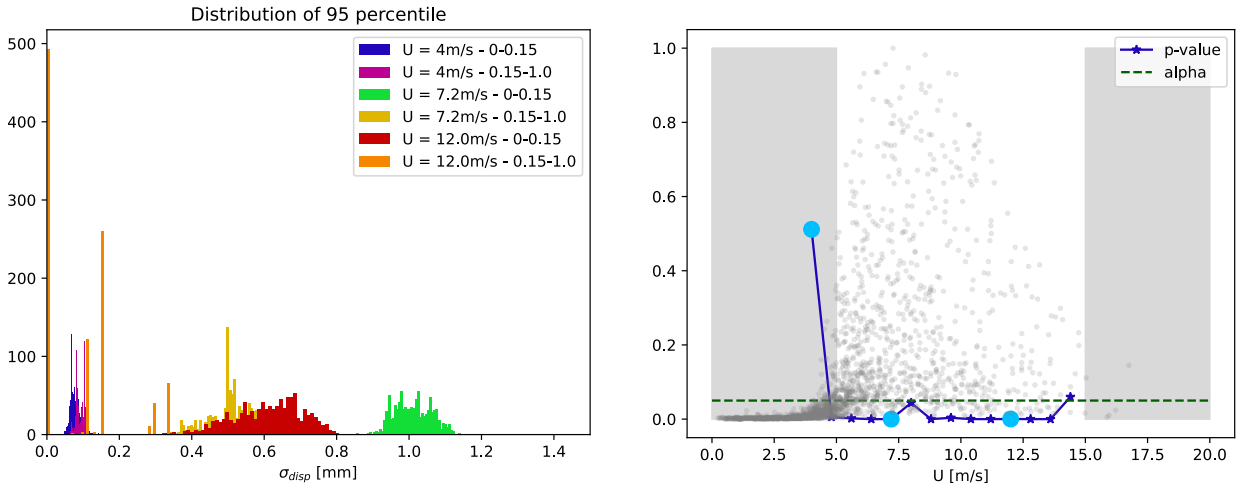

(a) (b)

Figure 26: a) Distribution of X^i_{95j} for $j = \{4m/s, 7.2m/s, 12m/s\}$ and $i = \{0-0.15, 0.15-1\}$. b) p-values for turbulence intensity comparison. In the background, the two sets of points are shown to guide the eye. Light blue dots indicate the configurations for which the distributions are detailed in Fig. 26a.

5. Conclusions

This study presents a statistical analysis of long-term hanger vibration data from the Hålogaland Bridge. The primary focus has been on evaluating the response of the bridge's three longest hangers, with findings indicating that their behaviour is predominantly caused by vortex-induced vibration. Key insights were gained by analyzing time histories from a hanger without dampers, revealing that constant mean wind velocity and bounded wind direction are essential but not sufficient for a single-mode lock-in VIV. The process of entering and exiting lock-in is complex and appears to be influenced by factors beyond just wind speed and direction changes. The hangers' frequency spectrum is characterized by multi-frequency vibrations, frequently shifting around the Strouhal frequency, instead of a stable mono-harmonic state. Further, it is shown that installing one damper reduced VIV vibrations by 80%, but additional dampers had a marginal effect. Nevertheless, the incorporation of extra dampers could potentially decrease vibrations of the dampers themselves, consequently extending their fatigue life.

Turbulence intensity was found to significantly affect the maximum vibration amplitude during lock-in, with high turbulence disrupting vortex shedding and reducing maximum hanger displacement.

In the analysis of wind data, it was found that the slowly varying wind remains constant for less than three minutes in half of the observed instances. This is shorter than the typical time required for the complete development of lock-in vibrations. This characteristic is key to understanding why the distribution of the 10-minute averaged response vibration amplitudes across different wind speeds is highly skewed towards the smallest displacements, with occasionally larger peaks when the lock-in regime is reached.

A novel application of statistical hypothesis testing on experimental data is been used to confirm that the VIV backbone curve calculation is not reliant on the duration of the time interval used to compute the statistical indicators. This technique has also confirmed turbulence's impact on the VIV response backbone curve. Higher turbulence intensities lead to a lower VIV amplitude. Therefore, the variability in the V-A curves observed is associated with turbulence characteristics rather than potential challenges arising from the coexistence of multiple timescales in statistical processing. The presented methodology

could be straightforwardly applied to the calculation of different backbones curves than the 95^{th} one. It can be also used to test the influence of different external parameters on the capability to correctly reconstruct these curves from experimental data for different wind velocities.

This study highlights the discrepancies between the complex VIV behaviour observed in field data and the prevailing theoretical models of VIV. It emphasizes the need for broadening our knowledge about VIV phenomena, particularly in practical applications for long-span suspension bridges.

CRediT authorship contribution statement

Giacomo Bacci: Formal analysis, Software, Visualization, Writing – Original Draft, Data Curation, **Øyvind Wiig Petersen**: Supervision, Writing – Review & Editing, Visualization, **Vincent Denoël**: Conceptualization, Supervision, Methodology, **Ole Øiseth**: Conceptualization, Supervision, Founding acquisition, Project administration.

Acknowledgements

This research was financially supported by the Norwegian Public Roads Administration. The authors appreciate this support.

References

[1] A. Abdel-Ghaffar, R. Scalan, Ambient Vibration Studies of Golden Gate, Journal of Engineering Mechanics 111 (1985) 463–482.

[2] A. Jamal, E. Sundet, Hålogaland Bridge—A Landmark in Arctic Norway, Structural Engineering International 31 (2021) 516–522. doi:10.1080/10168664.2021.1924100.

[3] A. Larsen, K. G. Andersen, A. Jamal, Wind Induced Hanger Vibrations–the Hålogaland Suspension Bridge, Structural Engineering International 32 (2022) 62–70. doi:10.1080/10168664.2021.1930332.

[4] M. Jafari, F. Hou, A. Abdelkefi, Wind-induced vibration of structural cables, Nonlinear Dynamics 100 (2020) 351–421. doi:10.1007/s11071-020-05541-6.

[5] G. Parkinson, Phenomena and modelling of flow-induced vibrations of bluff bodies, Progress in Aerospace Sciences 26 (1989) 169–224. doi:10.1016/0376-0421(89)90008-0.

[6] T. Sarpkaya, Vortex-Induced Oscillations, Journal of Applied Mechanics 46 (1979) 241–258.

[7] T. Sarpkaya, A critical review of the intrinsic nature of vortex-induced vibrations, Journal of Fluids and Structures 19 (2004) 389–447. doi:10.1016/J.JFLUIDSTRUCTS.2004.02.005.

[8] P. W. Bearman, Vortex Shedding from Oscillating Bluff Bodies, Annual Review of Fluid Mechanics 16 (1984) 195–222. URL: https://www.annualreviews.org/doi/10.1146/annurev.fl.16.010184.001211. doi:10.1146/annurev.fl.16.010184.001211.

[9] J. H. Lienhard, Synopsis of lift, drag, and vortex frequency data for rigid circular cylinders, 1966.

[10] C. Feng, The measurement of vortex induced effects in flow past stationary and oscillating circular and D-section cylinders, Ph.D. thesis, National Taiwan University, 1968.

[11] R. E. D. Bishop, A. Y. Hassan, The lift and drag forces on a circular cylinder oscillating in a flowing fluid, Proceedings of the Royal Society of London. Series A. Mathematical and Physical Sciences 277 (1964) 51–75. doi:10.1098/rspa.1964.0005.

[12] T. Staubli, Calculation of the vibration of an elastically mounted cylinder using experimental data from forced oscillation., Journal of Fluids Engineering 105 (1981) 225–229.

[13] Y. Tamura, Mathematical models for understanding phenomena: Vortex-induced vibrations, Japan Architectural Review 3 (2020) 398–422. doi:10.1002/2475-8876.12180.

[14] M. L. Facchinetti, E. de Langre, F. Biolley, Coupling of structure and wake oscillators in vortex-induced vibrations, Journal of Fluids and Structures 19 (2004) 123–140. doi:10.1016/J.JFLUIDSTRUCTS.2003.12.004.

[15] R. T. Hartlen, I. G. Currie, Lift-Oscillator Model of Vortex-Induced Vibration, Journal of the Engineering Mechanics Division 96 (1970) 577–591. doi:10.1061/JMCEA3.0001276.

[16] V. Denoël, Derivation of a slow phase model of vortex-induced vibrations for smooth and turbulent oncoming flows, Journal of Fluids and Structures 99 (2020). doi:10.1016/J.JFLUIDSTRUCTS.2020.103145.

[17] B. Fazl Ehsan, R. H. Scanlan, Vortex-induced vibration of flexible bridges, Journal of Engineering Mechanics 116 (1990) 1392–1411. URL: https://doi.org/10.1061/(ASCE)0733-9399(1990)116:6(1392).

[18] B. J. Vickery, R. I. Basu, Across-wind vibrations of structures of circular cross-section. Part I. Development of a mathematical model for two-dimensional conditions, Journal of Wind Engineering and Industrial Aerodynamics 12 (1983) 49–73. URL: https://www.sciencedirect.com/science/article/pii/0167610583900806. doi:10.1016/0167-6105(83)90080-6.

[19] R. D. Gabbai, H. Ã. Benaroya, An overview of modeling and experiments of vortex-induced vibration of circular cylinders, Journal of Sound and Vibration 282 (2005) 575–616. doi:10.1016/j.jsv.2004.04.017.

[20] Y. Deng, S. Li, . M. Zhang, . Xu Lei, Z. Chen, M. Asce, Wake-Induced Vibrations of the Hangers of the Xihoumen Bridge, Journal of Bridge Engineering 26 (2021). doi:10.1061/(ASCE)BE.1943-5592.0001779.

[21] Y. Fujino, K. Kimura, H. Takana, Wind resistant design of bridges in Japan: developments and practices, Springer Science & Business Media, 2012.

[22] E. Hjorth-Hansen, E. Strømmen, Wind-excited vibration of the longest suspenders of a suspension bridge., in: Proceedings of the 5th ISCD, St. Margherita, 2003, pp. 541–543.

[23] D. Zuo, N. P. Jones, J. A. Main, Vortex-and rain–wind-induced stay cable vibrations in a three-dimensional environment, in: 5th Int. Colloquium on Bluff Body Aerodynamics and Applications (BBAAV), Ottawa, 2004, pp. 397–400.

[24] E. d. S. Caetano, Veterans Memorial and Fred Harman Bridge (Texas), in: Cable Vibration in Cable-Stayed Bridges, International Association for Bridge and Structural Engineering, 2007, pp. 114–119.

[25] T. Argentini, L. Rosa, A. Zasso, Experimental evaluation of Hovenring bridge stay-cable vibration, WIT Transactions on Modelling and Simulation 55 (2013) 427–437. doi:10.2495/CMEM130351.

[26] I. F. Lazar, S. A. Neild, D. J. Wagg, Vibration suppression of cables using tuned inerter dampers, Engineering Structures 122 (2016) 62–71. URL: http://dx.doi.org/10.1016/j.engstruct.2016.04.017. doi:10.1016/j.engstruct.2016.04.017.

[27] H. Niu, Z. Chen, X. Lei, X. Hua, Development of eddy current turned mass damper for suppressing windinduced vibration of bridge hangers, 6th European and African Conference on Wind Engineering, EACWE 2013 (2013).

[28] S. Li, W. Gao, D. Yurchenko, X. Wang, J. Wang, X. Liu, Novel spacer-tuned-mass-damper system for controlling vibrations of hangers, Mechanical Systems and Signal Processing 167 (2022). doi:10.1016/j.ymssp.2021.108537.

[29] H. Wagner, V. Ramamurti, R. V. Sastry, K. Hartmann, Dynamics of stockbridge dampers, Journal of Sound and Vibration 30 (1973) 207–220. doi:10.1016/S0022-460X(73)80114-2.

[30] N. Barbieri, R. Barbieri, Dynamic analysis of stockbridge damper, Advances in Acoustics and Vibration 2012 (2012). doi:10.1155/2012/659398.

[31] M. Markiewicz, Optimum dynamic characteristics of stockbridge dampers for dead-end spans, Journal of Sound and Vibration 188 (1995) 243–256. doi:10.1006/jsvi.1995.0589.

[32] G. Diana, A. Cigada, M. Belloli, M. Vanali, Stockbridge-type damper effectiveness evaluation: Part I - Comparison between tests on span and on the shaker, IEEE Transactions on Power Delivery 18 (2003) 1462–1469. doi:10.1109/TPWRD.2003.817797.

[33] F. Foti, L. Martinelli, Hysteretic Behaviour of Stockbridge Dampers: Modelling and Parameter Identification, Mathematical Problems in Engineering 2018 (2018). doi:10.1155/2018/8925121.

[34] F. Di, L. Sun, L. Qin, L. Chen, Y. Zou, L. Jiang, Y. Zhu, Full-Scale Experimental Study on Vibration Control of Bridge Suspenders Using the Stockbridge Damper, Journal of Bridge Engineering 25 (2020) 1–10. doi:10.1061/(asce)be.1943-5592.0001591.

[35] X. Luo, L. Wang, Y. Zhang, Nonlinear numerical model with contact for Stockbridge vibration damper and experimental validation, JVC/Journal of Vibration and Control 22 (2016) 1217–1227. doi:10.1177/1077546314535647.

[36] M. Gu, X. Du, Experimental investigation of rain-wind-induced vibration of cables in cable-stayed bridges and its mitigation, Journal of Wind Engineering and Industrial Aerodynamics (2004). doi:10.1016/j.jweia.2004.09.003.

[37] J. OWEN, P. BEARMAN, A. SZEWCZYK, Passive control of VIV with drag reduction, Journal of Fluids and Structures 15 (2001) 597–605. URL: https://linkinghub.elsevier.com/retrieve/pii/S088997460090358X. doi:10.1006/jfls.2000.0358.

[38] W. L. Chen, D. B. Xin, F. Xu, H. Li, J. P. Ou, H. Hu, Suppression of vortex-induced vibration of a circular cylinder using suction-based flow control, Journal of Fluids and Structures 42 (2013) 25–39. doi:10.1016/J.JFLUIDSTRUCTS.2013.05.009.

[39] S. K. Patil, T. T. Ng, Control of Separation Using Spanwise Periodic Porosity, https://doi.org/10.2514/1.43321 48 (2012) 174–187. URL: https://arc.aiaa.org/doi/10.2514/1.43321. doi:10.2514/1.43321.

[40] Z. Li, I. M. Navon, M. Y. Hussaini, F. X. Le Dimet, Optimal control of cylinder wakes via suction and blowing, Computers and Fluids 32 (2003) 149–171. doi:10.1016/S0045-7930(02)00007-5.

[41] J. Fransson, P. Konieczny, P. Alfredsson, Flow around a porous cylinder subject to continuous suction or blowing, Journal of Fluids and Structures 19 (2004) 1031–1048. URL: https://linkinghub.elsevier.com/retrieve/pii/S0889974604000982. doi:10.1016/j.jfluidstructs.2004.06.005.

[42] A. J. Persoon, K. Noorlander, Full scale measurements on the Erasmus Bridge after rain/windinduced cable vibration, Proceedings of the 10thInternational Conference on Wind Engineering, Copenhagen, Denmark,1999 (1999) 1019–1026.

[43] S. Kim, S. Kim, H. K. Kim, High-mode vortex-induced vibration of stay cables: monitoring, cause investigation, and mitigation, Journal of Sound and Vibration 524 (2022) 116758. doi:10.1016/j.jsv.2022.116758.

[44] J. A. Main, N. P. Jones, Evaluation of Viscous Dampers for Stay-Cable Vibration Mitigation, Journal of Bridge Engineering 6 (2001) 385–397. doi:10.1061/(ASCE)1084-0702(2001)6:6(385).

[45] D. Cantero, O. Øiseth, A. Rønnquist, Indirect monitoring of vortex-induced vibration of suspension bridge hangers, Structural Health Monitoring 17 (2018) 837–849. doi:10.1177/1475921717721873.

[46] A. Larsen, Vibration Excitation and Damping of Suspension Bridge Hanger Cables, in: V. Gattulli, M. Lepidi, L. Martinelli (Eds.), Dynamics and Aerodynamics of Cables. ISDAC 2023. Lecture Notes in Civil Engineering, Springer, Cham, 2024, pp. 217–227. doi:https://doi.org/10.1007/978-3-031-47152-0_19.

[47] Ø. W. Petersen, G. T. Frøseth, O. Øiseth, Design and deployment of a monitoring system on a long-span suspension bridge, International Conference on Structural Health Monitoring of Intelligent Infrastructure: Transferring Research into Practice, SHMII 2021-June (2021) 1813–1817.

[48] S. Oh, E. Kim, D. Jung, Development of a Time-Domain Simulation Code for Cross-Flow Vortex-Induced Vibrations of a Slender Structure with Current Using the Synchronization Model, Journal of Marine Science and Engineering 10 (2022). doi:10.3390/jmse10121815.